WATER RESOURCES RESEARCH, VOL. 49, 2056–2067, doi:10.1002/wrcr.20196, 2013

On the fabrication of PDMS micromodels by rapid prototyping, and their use in two-phase flow studies

N. K. Karadimitriou,[1] M. Musterd,[2] P. J. Kleingeld,[1] M. T. Kreutzer,[2] S. M. Hassanizadeh,[1] and V. Joekar-Niasar[1]

Received 22 August 2012; revised 4 March 2013; accepted 13 March 2013; published 23 April 2013.

[1] Micromodels have been increasingly employed in various ways in porous media research, to study the pore-scale behavior of fluids. Micromodels have proven to be a valuable tool by allowing the observation of flow and transport at the micron scale in chemical, biological, and physical applications. They have helped to improve our insight of flow and transport phenomena at both microscale and macroscale. Up to now, most micromodels that have been used to study the role of interfaces in two-phase flow were small, square, or nearly square domains. In this work, an elongated PDMS micromodel, bearing a flow network with dimensions 5×30 mm^2 was manufactured. The pore network was designed such that the REV size was around 5×7 mm^2. So, our flow network was considered to be nearly four times the REV size. Using such micromodels, we established that the inclusion of interfacial area between the wetting and the nonwetting fluids models the hysteretic relationship between capillary pressure and saturation in porous media. In this paper, we first present the procedure for manufacturing PDMS micromodels with the use of soft lithography. Then, we describe an innovative and novel optical setup that allows the real-time visualization of elongated samples. Finally, we present the results obtained by quasi-static, two-phase flow experiments.

Citation: Karadimitriou, N. K., M. Musterd, P. J. Kleingeld, M. T. Kreutzer, S. M. Hassanizadeh, and V. Joekar-Niasar (2013), *Water Resour. Res.*, *49*, 2056–2067, doi:10.1002/wrcr.20196.

1. Introduction

[2] In porous media research, micromodels have been increasingly employed in various ways, to study the pore-scale behavior of fluids. Micromodels have proven to be a valuable tool by allowing the observation of flow and transport at the micron scale in chemical, biological, and physical applications. They have helped to improve our insight of flow and transport phenomena at both microscale and macroscale.

[3] An overview of various issues related to micromodels, such as network generation, fabrication materials and methods, visualization methods, and different applications, was given in *Karadimitriou and Hassanizadeh* [2012]. They defined a micromodel as "an artificial representation of a porous medium, made of a transparent material. This fluidic device bears a flow-network, with features on the microscale, and an overall size of up to a few centimeters."

[4] Micromodels have been mostly used in studying displacements of two immiscible fluid phases in porous media [*Chang et al.*, 2009; *Corapcioglu et al.*, 2009; *Avraam et al.*, 1994; *Baouab et al.*, 2007, *NagaSiva et al.*, 2011]. Processes of drainage and imbibition, as well as the mechanisms that dominate them, like viscous or capillary fingering, snap-off, etc., have been studied using micromodels [*Zhang et al.*, 2011; *Ferer et al.*, 2004; *Grate et al.*, 2010; *Gutiérrez et al.*, 2008; *Hug et al.*, 2003; *Huh et al.*, 2007].

[5] Recently, two-phase flow studies were performed using photo-resist micromodels that had flow patterns based on stratified percolation [*Cheng*, 2002; *Pyrak-Nolte et al.*, 2008; *Cheng et al.*, 2004, 2007; *Liu et al.*, 2011]. In these studies, distributions of the two phases in the flow network during quasi-static drainage and imbibition were visualized. Phase saturation and interfacial area could be determined using image processing and relationship between phase saturation, capillary pressure, and specific interfacial area was investigated.

[6] Micromodels have been made of different materials with their advantages and disadvantages. A detailed account of these issues can be found in *Karadimitriou and Hassanizadeh* [2012]. One important property of micromodels is wettability. Glass or quartz micromodels are uniformly and stably hydrophilic, which is a major advantage. Also, using deep reactive-ion etching method, vertical pore walls can be created (which is usually desired), as long as the pores depth is less than 30 μm deep. For larger pore depth, DRIE results in sloped walls; the slope being larger for bigger depth [*Ohara et al.*, 2010; *Yeom et al.*, 2005; *Karadimitriou et al.*, 2012]. Deeper pores can be created in glass using chemical etching [*Johnston*, 1962; *Wegner and*

[1]Earth Sciences Department, Utrecht University, Utrecht, Netherlands.
[2]Chemical Engineering Department, Delft University of Technology, Delft, Netherlands.

Corresponding author: N. K. Karadimitriou, Earth Sciences Department, Utrecht University, Budapestlaan 4, 3584 CD, Utrecht, Netherlands. (N.K.Karadimitriou@uu.nl)

©2013. American Geophysical Union. All Rights Reserved.
0043-1397/13/10.1002/wrcr.20196

Christie, 1983; *McKellar abd Wardlaw*, 1982; *Er et al.*, 2010], but then pore walls will be curved at the bottom, as the erosion process is highly isotropic. Silicon micromodels have the disadvantage that the pore walls are made of two materials. The pore network is created in silicon but, because silicon is not transparent, the micromodel is usually covered by a glass plate [*NagaSiva et al.*, 2011; *Baumann and Werth*, 2004; *Willingham et al.*, 2008]. This results in a mixed wettability. Photo-resist micromodels have the advantage that they are relatively easy to make, but only in a special clean room environment. Also, they are sensitive to ultra-violet light; so that nitrogen is produced under regular light, which eventually destroys the network. Moreover, photo-resist micromodels gradually degenerate after a number of uses.

[7] A transparent material often used for microfluidic devices is Poly-Di-Methyl-Siloxane (PDMS). PDMS is a viscoelastic, silicon-based organic polymer. It is optically transparent, inert, nontoxic, and nonflammable. PDMS is hydrophobic in its natural state. But, this hydrophobicity is variable in time and space [*Murakami et al.*, 1998; *Fritz and Owen*, 1995]. This is a major disadvantage. However, we have developed a treatment process in order to make PDMS surface wettability uniform and stable. A solution of Trichloro-perfluoro-octyl-silane (silane in short) in 96%-pure ethanol was injected through a filter into the micromodel, so as to change its surface chemistry and make it uniformly and strongly hydrophobic.

[8] PDMS is a material which is easy and safe to use in a normal laboratory environment. PDMS micromodels are relatively cheap to make and are reusable almost without limit. Finally, the geometrical characteristics of the features of the micromodel can easily be very well controlled, as it will be shown later in this paper.

[9] Up to now, most micromodels that have been used to study flow and transport in porous media, including interfacial area as a separate state variable, were small, (nearly) square domains, so that they could be visualized under a microscope. Therefore, one may interpret them as being one Representative Elementary Volume (REV). An REV is the volume of a homogeneous porous medium above which the system properties are insensitive to the averaging domain size. Often, only one average value for porosity, saturation, or capillary pressure is given for the whole micromodel. In the present work, an elongated micromodel with dimensions 5×30 mm^2 was manufactured. The pore network was designed such that the REV size was around 5×7 mm^2 (the determination of REV size is explained in section 2.2). So, our micromodel was considered to be nearly four times the REV size. A long micromodel is similar to a column experiment; one can determine gradients in saturation, capillary pressure, and interfacial area. But, then a microscope is not suitable for real-time visualization of a long micromodel under transient flow conditions. Therefore, we have designed and constructed an innovative and novel optical setup using digital cameras, for observing and imaging fluids distribution along the whole model at any given time.

[10] Through performing experiments in such micromodels, we investigated the role of fluid-fluid interfaces in the hysteretic relationship between capillary pressure and saturation in porous media. With this work, we provide experimental evidence to support the theories which propose that for a complete description of two- or multiphase flow, interfacial area should be included as one of the state variables, in addition to pressure and saturation [*Hassanizadeh and Gray*, 1990, 1993a, 1993b].

[11] In this paper, we first present the procedure for manufacturing PDMS micromodels with the use of soft lithography [*Xia and Whitesides*, 1998; *Duffy et al.*, 1998]. Then, we describe our visualization setup that allowed the real-time visualization of elongated samples. Finally, we present the results obtained from quasi-static, two-phase flow experiments.

2. Construction of the Micromodel

2.1. Main Steps

[12] A micromodel is commonly composed of two slabs. One slab contains the pore network and the other slab, which is featureless, is used as a cover. This creates a closed network of pores. The manufacturing process of our PDMS micromodel consisted of a number of steps, which are briefly mentioned here and explained in detail in the following subsections. First, the flow network was designed, as well as the inlet and the outlet areas. This design was transferred to a mask. The mask was a plastic transparency sheet with the flow network and reservoirs being transparent and in their actual dimensions, and the solid phase being black. It was used in the process of creating a patterned silicon wafer that would serve as a mold. This wafer, usually called the "master", was used for the preparation of a PDMS slab with the network and the two reservoirs formed in it. Another PDMS slab without any features was then used to cover the micromodel. Finally, the micromodel was treated in order to acquire a uniform wettability. These manufacturing steps will be explained in detail shortly.

2.2. Design of the Flow Network and the Reservoirs

[13] An elongated pore network with an overall size of 5×30 mm^2 was designed. The pore network was represented by an assembly of pore bodies and pore throats with a wide distribution of sizes. The network topology was generated using Delaunay triangulation, which is considered to provide a good representation of real porous media [*Heiba et al.*, 1992]. In the Delaunay triangulation, points are connected to their neighbors by nonintersecting bonds. Connected points form triangles that are as equilateral as possible. The coordinates of the triangulation points were generated by the use of a fixed routine in MatLab. These points were considered to be the centers of pore bodies. The number of pore bodies directly connected to a pore body, which is usually called the coordination number, was not constant throughout the whole network; it varied from 4 to 6 for the 2000-points network, from 5 to 8 for the 3000-points network, and from 6 to 9 for the 6000-points network.

[14] Pore bodies were cylinders and the pore throats were parallelepipeds. In planar view, pore bodies were circular while pore throats were rectangular. They had the same depth and had a rectangular cross section.

[15] Pore body sizes were assigned from a truncated log-normal distribution. The length of a pore throat was defined

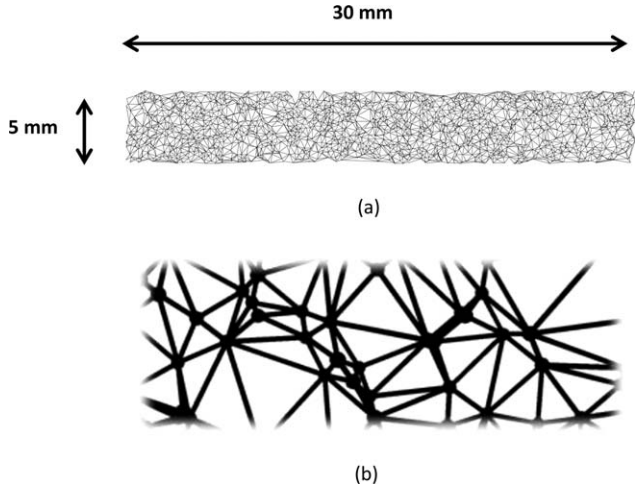

Figure 1. (a) Image of the pore-network with 2000 pore bodies and 6000 pore throats and a mean pore size of 40 μm. The void space is shown in black. (b) Zoomed-in image of a part of the network.

as the distance between two connected pore bodies, minus the sum of their radii. The width of a pore throat was assigned by using the following set of equations [*Joekar-Niasar et al.*, 2010a]:

$$r_{ij}=\rho_i\rho_j\left(\rho_i^{\frac{1}{n}}+\rho_j^{\frac{1}{n}}\right)^{-n}, n>0, r_{ij}={}^{w_{ij}}/_{d}, \tilde{R}_i={}^{R_i}/_{d}, \rho_i=\frac{\tilde{R}_i\sin(\pi/4)}{\left(1-\tilde{R}_i\cos(\pi/4)\right)^n} \quad (1)$$

where R_i is the radius of pore body i, w_{ij} is the width of the pore throat ij, and d is the distance between the two centers. In this formula, n is an extra tuning parameter for specifying the pore throat size. It also makes sure that the width of the pore throat would always be smaller than the diameter of the smallest pore body that it is connected to.

[16] In Figure 1, the whole network as well as a magnified image of part of it can be seen. The pore network was designed such that the REV size was around 5×7 mm^2. So, our micromodel was considered to be nearly four times the REV size. The REV size was determined through pore-network modeling as follows. Simulations were run for the whole extent of the micromodel. Then, capillary pressure-saturation curves under quasi-static conditions were obtained for a sequence of gradually increasing subdomain sizes and compared to each other. The subdomain size beyond which the capillary pressure-saturation curve remained unchanged was considered to be the REV size.

[17] For the introduction of each phase into the flow network, two reservoirs, one for each phase, were designed at the beginning and the end of the flow network. Special attention was paid to the design of the reservoirs. They were much bigger than the size of a single pore body, whereas their height was the same as the rest of the model. This created a very high ratio between the width and the height of the reservoir. This consequently led to the collapse of the top surface and blocking of the flow in an earlier design of the micromodel. In fact, *Bietsch and Michel* [2000] have shown that there is a maximum ratio between the distance separating two sequential features in PDMS, and their height, as well as between the void space between these features and their own volume. So, pillars were added to support the reservoir's top surface and prevent it from collapsing. In Figure 2, the reservoir can be seen, where the void space is shown in black and the PDMS pillars are in white. The large difference in the size of pores of the micromodel and the reservoir are also evident in this figure.

[18] The Autocad drawing of the flow network with the two reservoirs, was then sent to the CAD/Art Company (Oregon, U.S.A.), in order to create a mask at a resolution of 20,000 dots per inch.

2.3. Preparation of a Patterned Silicon Wafer With Photo-Lithography

[19] A necessary step in the manufacturing process of PDMS micromodels was the preparation of a silicon wafer that bore the features of the micromodel (flow network and reservoirs) and would be used as a mold. This wafer is usually called the "master".

[20] For this purpose, first, the silicon wafer was put in an oven for 15 min, at 120°C. This was done in order to remove any moisture from the surface of the wafer that might harm the adhesion process later on in the process. The wafer was then spin coated with SU8 2025 photoresist. It was put on a spin coater and a small portion of photoresist was poured on it. The choice of rotation speed and time depends on the desired depth of the photo-resist layer, which had to be the same as the depth of the flow network. Calibration curves were provided by the supplier of the photoresist. For example, to achieve a thickness of 40 μm, the wafer was put to spin for 90 s at a rotation rate of 2000 rounds per minute. Then, the wafer was put on a hotplate and was soft-baked at 65°C for 3 min, and immediately after that at 95°C for 6 min. In this way, the photoresist became harder and degassed, photo-sensitive, but not yet solid. Right after this step, the wafer and the mask (which contained the flow network and the two reservoirs), were put under an aligner, where they were illuminated by ultraviolet light. Parts of the photoresist-coated surface of the wafer that were visible through the mask open areas were exposed to the light. Depending on the height of the photoresist layer, the energy level of the light beam had to be tuned to penetrate the thickness of the photo-resist layer,

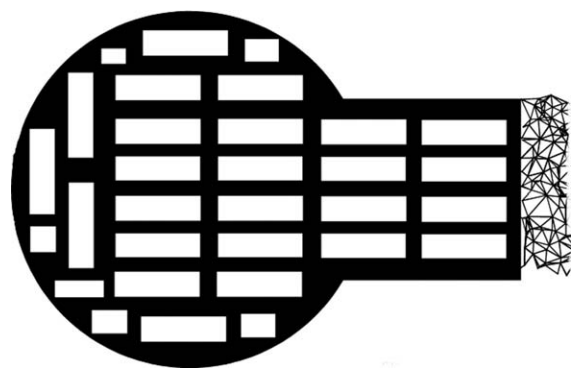

Figure 2. The schematic of the reservoir with the supporting pillars. The void space is shown in black and pillars in white.

according to the specifications of the photo-resist supplier. As soon as this step was finished, the wafer was hard baked on a hot plate at 65°C for 1 min and immediately after that at 95°C for 6 min to allow cross linking of the exposed photoresist. The wafer was then put in a glass Petri dish and was covered with Mr-dev 600 developer liquid (micro resist technology GmbH). By gently moving the Petri dish with the wafer in it for approximately 10 min, the photo-resist areas that were not exposed to the ultra-violet light were dissolved. This led to the features of the network and the reservoir to be formed on the wafer.

[21] In this way, a wafer was made that could be used as a mold to make replicates of the same network (as explained in the next section). This part of the process of the manufacturing of PDMS requires a clean room environment. The whole operation was performed in the class-10000 clean room facility of the Kavli Institute of Nanoscience Delft. The rest of the process was carried out in our regular laboratory.

[22] In our regular laboratory, the master was then put in a vacuum chamber and was silanized. A droplet of silane was put in the vacuum chamber; it evaporated and formed a monolayer on the surface of the master that prevented the PDMS from adhering to the master's surface. In this way, PDMS could be easily peeled off the wafer, without leaving any residues. If an unsilanized master is used, then the photo-resist features on the master would be peeled off together with the PDMS slab.

2.4. Fabrication of a PDMS Micromodel

[23] The raw materials that were needed to make a PDMS micromodel were a silicon elastomer base (Dow Corning Slygard 184), and the corresponding elastomer curing agent. The silicon elastomer base, which was in liquid state, was mixed with the elastomer curing agent at a mass ratio of 10:1. The two components were mixed thoroughly by stirring them in a cup for a few minutes. The quantity of PDMS that was used, determined the thickness of the slabs created. In our work, typical values for the weights of the two components were 50 g and 5 g, respectively. The resulting amount of PDMS would make sure that the PDMS slabs were thick enough to create a relatively rigid micromodel. Also, it was thin enough for the inlet and outlet holes to be punched without creating cracks in the material.

[24] After mixing, the mixture was full of trapped air bubbles. So, the cups with the mixture were put into a vacuum chamber to remove the trapped air. It was important not to use the same vacuum chamber that was used for the silanization of the master, as it was already contaminated with silane. We released the vacuum suction periodically for two reasons. First, the degassing of the material was faster in the first 5 min of the process, and then it became slow. Second, the rising trapped air would raise the level of the liquid in the cup. If the vacuum was not released, it would have spilled over the cup.

[25] After degassing, the content of one cup was poured over the master silicon wafer in a Petri dish, with the design of the micromodel pointing upward. The material had to be poured as slowly as possible in order to avoid having too much trapped air. It was also important not to pour PDMS directly on top of the features of the master wafer, but on the blank surface of the wafer, allowing the liquid PDMS to flow slowly into and over the flow network. Otherwise, there was a chance that dust particles become trapped in the main structure of the flow network, resulting in a defective micromodel.

[26] Next, a layer of PDMS was poured in another Petri dish to form a plain slab without any features. This PDMS slab was used as the sealing layer of the micromodel. Then, the two Petri dishes were put in the vacuum chamber to remove any trapped air.

[27] After degassing, the two Petri dishes were put in an oven at 68° for at least 2 h in order to cure and solidify liquid PDMS. In general, various combinations of temperature and curing time can be employed. The limit combinations are: more than 48 h in ambient temperature and 10 min at 200°. For the latter case, a glass Petri dish should be used, as a plastic one will deform because of the heat. However, longer curing times and less curing temperature are favorable to avoid creating stresses in the material. Ambient temperature is not a very good option as it takes too much time, and the material may be exposed to dust particles that may stick on its surface before it solidifies.

[28] After curing, the PDMS slabs were allowed to reach ambient temperature before bonding them. In this way, permanent distortions because of excessive stress on the material could be avoided.

[29] The PDMS slab had to be separated from the silicon wafer in a way that it would not destroy the wafer's features. First, with the use of a scalpel or sharp pointy knife, PDMS was cut around the wafer's edges and was gently removed from the Petri dish. The wafer was gently separated from PDMS. It was essential that this procedure was as slow as possible, so that the features on the wafer would not be detached from the wafer. The Petri dish that had only plain PDMS slab was much easier to handle. One just had to cut the edges and remove the PDMS slice from the Petri dish.

[30] Microscope glass slides (Menzel-Glaser) with dimensions of 76 mm x 26 mm were used as guides to cut the parts of PDMS slab containing the flow network and the two reservoirs. Pieces of the same size were also cut from the plain PDMS slab, which was to be used for sealing the micromodels. Inlet and outlet holes were punched into the middle of the reservoir areas of the slab with features using a leather hole punching tool.

[31] The two PDMS slabs had to be put together and bonded. The plain PDMS slab was placed in such a way that its surface that was in contact with the Petri dish would form the inner side of the micromodel. This ensured that the surface would be smooth and free of dust particles.

[32] There are various bonding techniques [*Eddings et al.*, 2008]. These techniques involve oxygen plasma [*Duffy et al.*, 1998, 1999], corona discharge [*Haubert et al.*, 2006], partial curing of PDMS in an oven [*Go and Shoji*, 2004; *Eddings and Gale*, 2006], use of a curing agent [*Samel et al.*, 2007], and stamp/stick [*Satyanarayana et al.*, 2005]. We tried two techniques: oxygen plasma and corona discharge. A discussion of these bonding methods and related issues is given below.

[33] For the oxygen plasma bonding, an Expanded Tabletop Plasma Cleaner (Sigma-Aldrich) was used. Typical values for control parameters of the oxygen cleaner

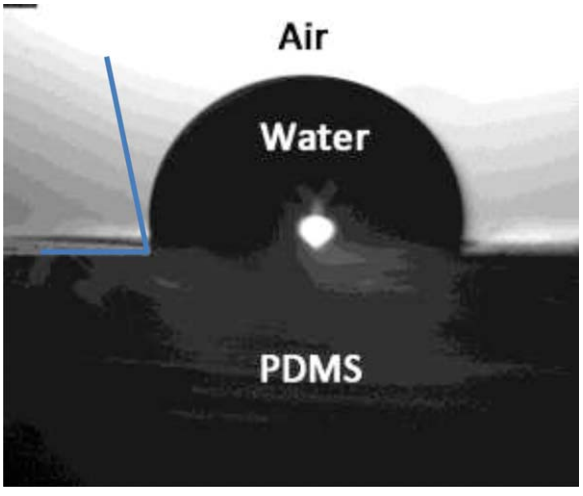

Figure 3. A water droplet in contact with PDMS and surrounded by air. Contact angle between air and PDMS is shown.

were a vacuum pressure of 0.3–0.4 mbar, output power of 30 W, and exposure time of up to 3 min.

[34] For corona bonding, there is no known recipe for obtaining specific results. We used a typical value for voltage of 15 kV. It was found that if the distance between the specimen and the treater was less than 4 cm, the bonding effect was more or less insensitive to the distance. As there was no guideline for the exposure time, a number of measurements were carried out to determine the optimal value. In this case, optimal meant that after bonding, the micromodel would withstand the highest possible applied pressure without any leakage. It was observed that the bonding strength was correlated to the contact angle of a droplet of water on top of PDMS after corona treatment. The lowest contact angle (measured on the air side; see Figure 3) seemed to correspond to a bonding with the maximum tolerance to the applied pressure. For a distance of 1.5 cm, different exposure times were tested and the contact angle was measured. Results of the measured contact angle for different exposure times are shown in Figure 4.

[35] These results show that the smallest contact angle is achieved at an exposure time of 25 s. So, this was the exposure time used in the bonding of micromodels.

[36] In both cases of oxygen plasma or corona discharge treatment, after exposure, the two parts of the micromodel were put together and a gentle mechanical pressure was applied to them until chemical bonding was achieved. Special attention was paid to removing the air trapped between the contacting surfaces of the two slides. This was achieved simply by applying some extra pressure on the relevant areas and expelling the air.

[37] In order to make the micromodel more rigid, using the same bonding procedure, a microscope glass slide (Menzel-Glaser) was bonded to the side of the micromodel that did not have inlet and outlet holes.

[38] For the bonding to mature, the model was left to rest for a few hours or, even better, put in the oven overnight at a moderate temperature ($\pm 68°$). This step was particularly important for the corona discharge bonding. Otherwise, bonding could be reversed.

3. Issues With PDMS Models

[39] In this section, we will explain how to solve a number of known issues related to the use of PDMS material in two-phase flow experiments.

3.1. Wettability Issues

[40] One of the most important properties of a micromodel is the wettability of its material. In two-phase flow studies, it is very important to have a uniform and stable wettability throughout its flow network. In our experiments, it did not matter whether the micromodel was hydrophobic or hydrophilic, as long as it remained uniformly and permanently in the same state. Hereunder, we describe the wettability problems of PDMS micromodels and explain how we achieved stable and uniform wettability properties.

[41] PDMS is hydrophobic in its natural state. But its wettability properties change during, and as a result of, the bonding process. For example, the oxygen plasma technique, introduced by *Duffy et al*. [1998], causes PDMS to become hydrophilic. *Duffy et al*. tried to enhance the bonding strength by activating layers of cross-linked PDMS, through surface oxidation. It is believed that surface oxidation exposes silanol groups (Si-OH) at the surface of the PDMS layers and, when brought together, they form covalent siloxane bonds (Si-O-Si). This process makes PDMS even more hydrophilic. However, the material returns to its original state when exposed to the atmosphere for some time (a few minutes to a few hours) [*Bodas and Khan-Malek*, 2007]. The corona discharge technique has an opposite effect, compared to oxygen plasma treatment. It makes the material more hydrophobic than its natural state. But also in this case, PDMS returns to its original hydrophobicity level. Our PDMS micromodels, which were bonded by the oxygen plasma treatment technique, originally had a hydrophilic behavior, as expected. However, within a relatively short time (around 12 h after bonding), their wettability started to change gradually. After roughly three days, the material was hydrophobic with nonuniform

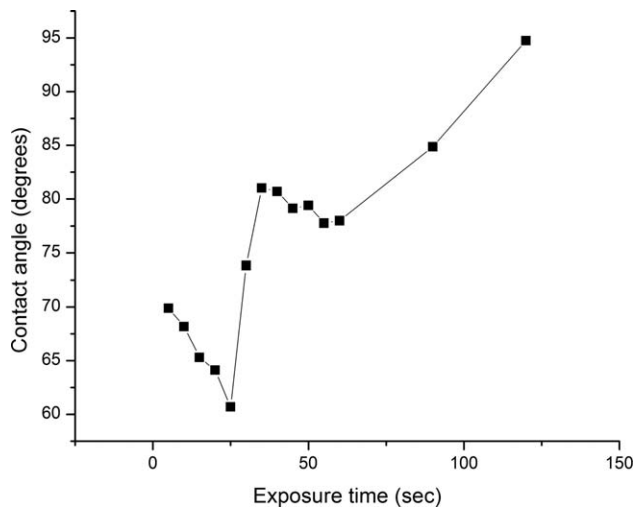

Figure 4. The air contact angle versus time of exposure to corona discharge. Note that because the contact angle is measured in the air, a contact angle of zero means that the surface is completely hydrophobic.

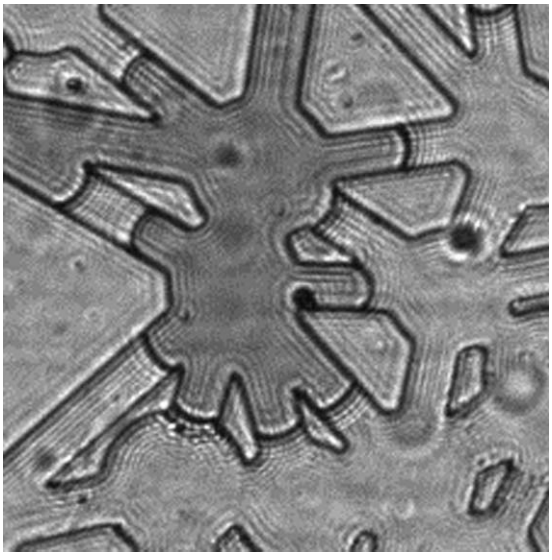

Figure 5. Snapshot taken from a part of the flow network filled with two immiscible liquids. In dark color is the nonwetting phase. The wetting phase is colorless. The contact angles varied from 80° to 60°.

wettability. In Figure 5, a magnified part of the network filled by two immiscible fluids can be seen. The snapshot was taken at equilibrium, so there is no further movement of the fluid-fluid interfaces. It is evident that there is mixed wettability even within a very small area. The contact angle between the phases was measured under static conditions with ImageJ software, and was found to vary from 80° to 60°. Even days after bonding, in some parts of the network, a mixed wettable condition was visible. This showed that the wettability of PDMS is a function of time, and is dependent on the initial wettability condition.

[42] Similar observations were made after treating the micromodel with corona discharge bonding, where the material was more hydrophobic than in its natural state.

[43] The wettability problem was solved by employing and improving a silanization technique. In this technique, a solution of silane in 96%-pure ethanol was injected through a filter. The pores of the filter were 0.45 μm wide. In this way, silicon, which a by-product of the reaction of TCP with water in ethanol and in the air, was kept out of the flow network, preventing blockage.

[44] A total volume of 1 ml of a 0.018 v/v solution was introduced into the micromodel at a pumping rate of 3 μl/min. Then, the model was put in an oven at 68°C overnight to dry out. After that, the micromodel was ready for use.

[45] After this silanization procedure, the micromodel network was uniformly hydrophobic everywhere. The phases used in this study were fluorinert as the wetting phase, and water dyed with ink as the nonwetting one. Fluorinert is a colorless (refraction index, $n = 1.291$), fluorine based, and inert liquid. It is 4.7 times more viscous ($\mu = 4.7 \times 10^{-3}$ Pa×s) and 1.86 times heavier than water ($\rho = 1860$ kg/m^3). The interfacial tension between water and Fluorinert is 58 mN/m.

[46] In Figure 6, a magnified part of the network can be seen during drainage. It is a snapshot taken under quasi-static conditions. Fluorinert is seen in light color and water in dark color. It is obvious that the water is the nonwetting phase, and fluorinert is the wetting one. The contact angles are clearly small everywhere. That was also cross checked with the use of ImageJ software to measure the contact angle from the image. Values between zero and 4° were found.

[47] The contact angle was also measured under pressure-free conditions as follows. A droplet of water was dropped in a beaker filled with fluorinert. As water is much lighter, it stayed on the surface. Then, a silanized PDMS slab was put on top of them. The contact angle between water, fluorinert, and PDMS was measured. We found it to be equal to 4°.

3.2. Deformation of Micromodel

[48] An issue that needs attention is the possibility of swelling of PDMS due to contact with organic liquids and its deformation under the pressures of liquids. PDMS swells when it comes in contact with nonpolar organic solvents, like hydrocarbons, toluene, and dichloromethane. *Lee et al*. [2003] examined the compatibility of organic liquid with PDMS. They stated that the problem of liquid compatibility has three aspects: 1) the absorption of the liquid in PDMS, and potential swelling of PDMS, 2) the diffusion of liquid components in PDMS, and 3) the dissolution of oligomers (swelling oils) in PDMS. In the work of *Dangla et al*. [2010], the dynamics of penetration of solvents in PDMS and its relation to volume dilation were studied in a model experiment, allowing a precise measurement of the diffusion coefficients of oils in PDMS. The two liquids that we used, water and fluorinert, do not cause swelling of PDMS. In general, alcohols, polar solvents, and fluorine-based fluids do not have a swelling effect on PDMS.

[49] In the work of *Gervais et al*. [2006], the effect of liquids pressure on the deformation of shallow microfluidic channels was examined. Such deformation can, in turn, affect the laminar flow profile and pressure distribution within the channels. They came up with a dimensionless number for assessing the significance of this deformation, depending on the pressure drop along a channel, its width and height, and the Young modulus of PDMS. Based on this dimensionless number, we determined that the deformation of PDMS in our experiments can be neglected.

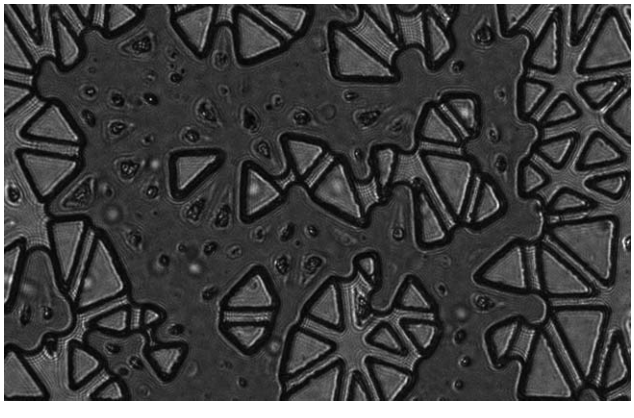

Figure 6. A magnified image of the network during drainage. The curvatures of the interfaces show a strong wettability of the medium to fluorinert (seen in light color).

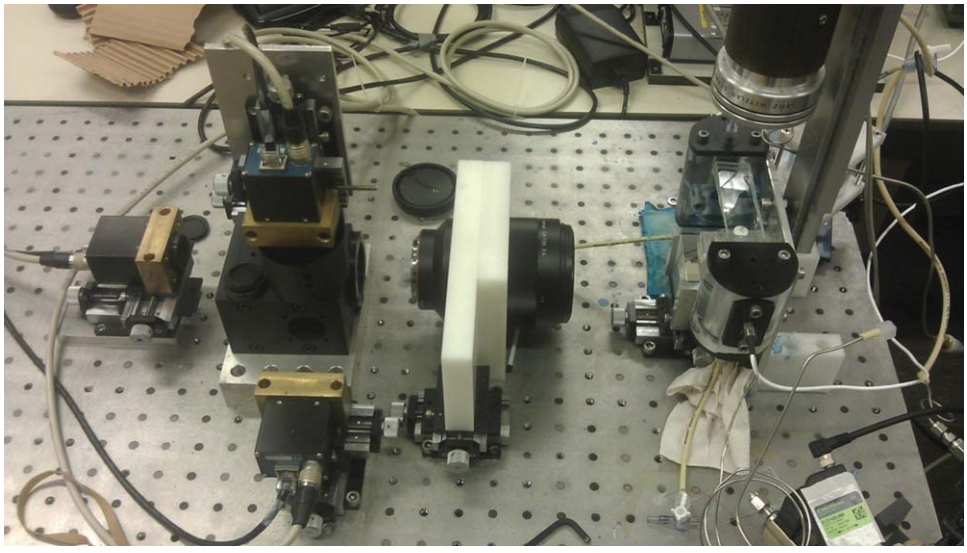

Figure 7. The experimental setup for the visualization of the elongated micromodel: (1) LED light source mounted with an objective lens. (2) Prism. (3) Magnifying lens. (4) Box with three beam splitters. (5) High-resolution CMOS cameras. The micromodel is labeled A and the inflow/outflow reservoirs are designated by B and C, respectively.

4. Experimental Setup

4.1. Visualization Setup

[50] In most micromodel studies, conventional microscopy is employed for visualization of pore-scale processes. But, this method would be inadequate for the visualization of our elongated flow network. The reasons are that with a conventional microscope, only a square part of the flow network can be visualized at a high resolution, at any given time. The rest of the model would be outside the field of view of the microscope. For this reason, we designed an innovative optical setup which allowed us to visualize and record images of the whole micromodel at any given time.

[51] A picture of the experimental setup is shown in Figure 7. Major components of the optical setup were: (1) a collimated LED light source mounted with an objective lens F 3.2/105 mm, (2) a prism (Edmund Optics) with dimensions of 50 mm × 50 mm, (3) a SONY Sonnar F1.8/135 mm magnifying lens, (4) a box containing three beam splitters (Edmund Optics) with dimensions of 35 mm × 35 mm, and (5) four 5-Megapixel Prosilica GC-2450 cameras. The micromodel (A) was placed horizontally on a stage between the light source and the prism. The input and output holes of the micromodel were aligned with the holes of an inflow reservoir (B) and an outflow reservoir (C), respectively. The whole setup was placed on a vibration-free optical table (Standa Opto-Mechanics). In Figure 8, a schematic representation of the visualization setup is shown.

[52] The working of the visualization setup was as follows. The collimated light passed through the micromodel,

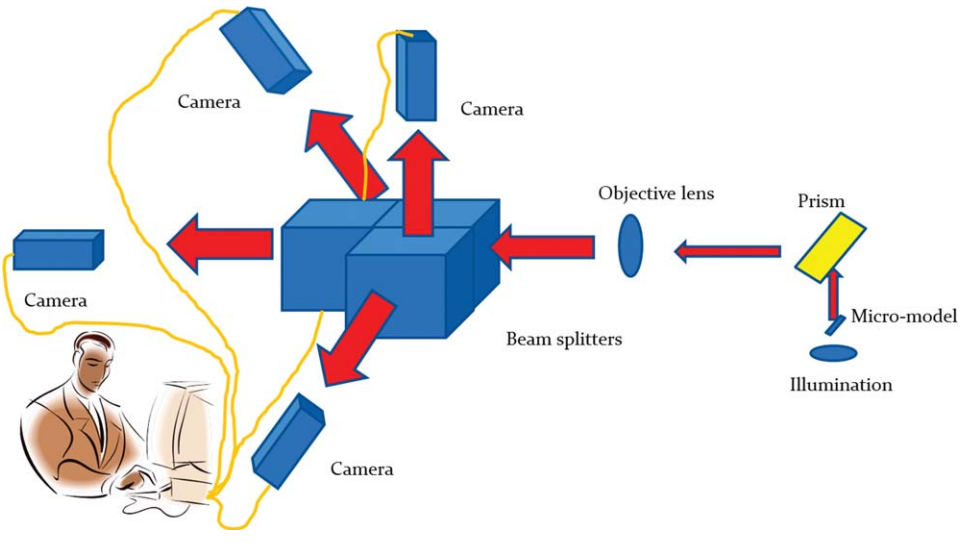

Figure 8. A schematic representation of the visualization setup.

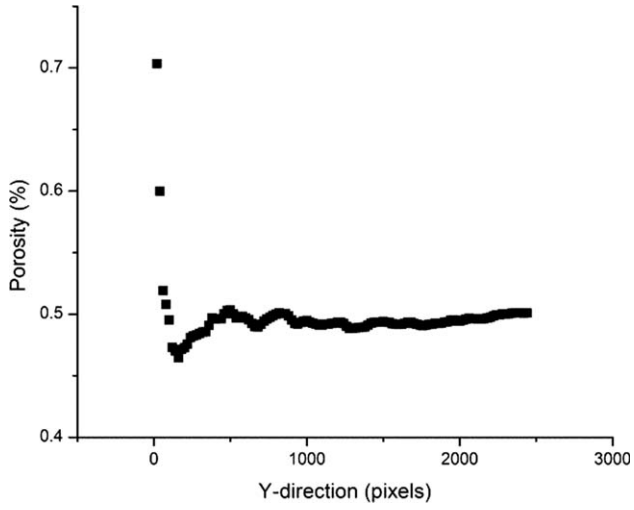

Figure 9. Porosity calculated for increasingly larger domain length. The width was kept equal to network width of 5 mm. Porosity reaches a constant value of 50% for domain sizes larger than ca 2.8 mm.

and it was bent by the prism to become parallel to the optical table. The beam splitters reproduced four identical images in four perpendicular directions. In each direction, there was a camera placed such that each camera received a different part of the image. By adding the images of all four cameras, the whole extent of the flow network could be visualized. The distance between the optical parts of the setup, as well as their optical properties (like focal length, numerical aperture of the lens, etc.) where carefully chosen, so that the final image that every camera would receive could fit exactly in the camera's sensor. The part of the micromodel recorded by each camera was about 5×7 mm^2. We confirmed that this corresponds to an REV, by determining the porosity over domains of 5 mm in width but increasingly larger length. We varied the averaging domain length from 56 μm (equivalent to 20 pixels) to 14 mm (see Figure 9). We see that for domains larger than 2.8 mm, the porosity is around 50%, which was also the porosity measured for the whole flow network. So, the REV size can be considered to be in the range above 2.8 mm.

[53] A detailed explanation of the visualization setup can be found in *Karadimitriou et al*. [2012]. In Figure 10, images from the four cameras of a network with dimensions of 5 mm $\times$ 30 mm are shown.

4.2. Pressure Measurement and Control

[54] The inflow and outflow of fluids were controlled through the two external reservoirs B and C. At exactly the same level as the level of the micromodel, two pressure

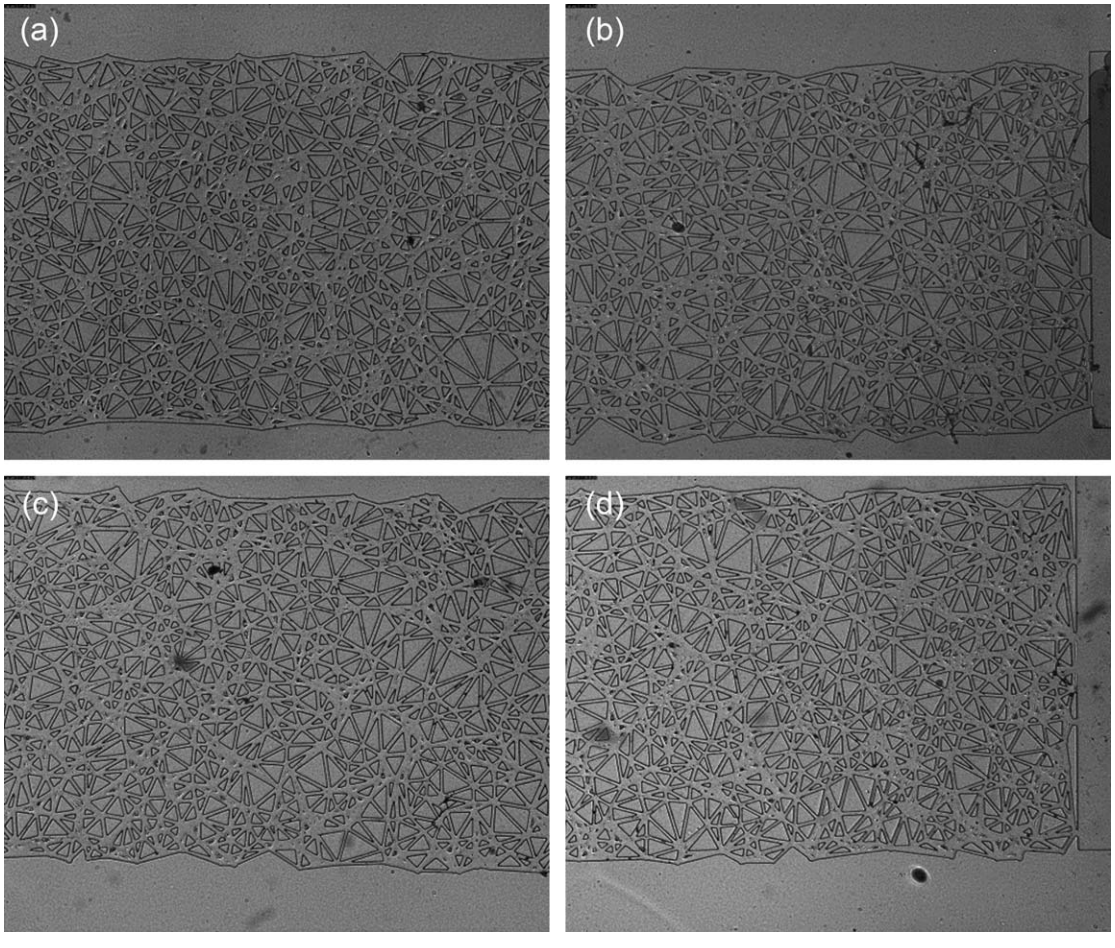

Figure 10. The four images of the flow network numbered according to their sequence in the micromodel. In total, the pictures cover an area of 5 mm $\times$ 30 mm, visualized at a resolution of 2.8 μm/pixel.

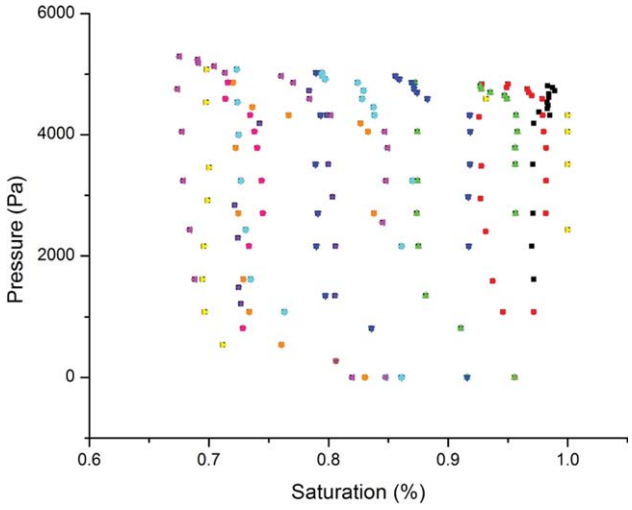

Figure 11. Capillary pressure as a function of Fluorinert saturation for primary drainage, main imbibition, and scanning curves.

transducers (Kulite XTL-190M-0,7B-D) were installed, one in each reservoir, to measure the fluid pressures. These transducers were connected to a differential pressure controller (Bronkhorst). The differential pressure controller had an RS-232 interface that was connected to a computer. In this way, it was possible to set, measure, and control the differential pressure between the two reservoirs at any instant. The controller was calibrated in a way that the maximum pressure difference would be 27 kPa with an accuracy of 25 Pa. The pressure controller could adjust the pressure in the nonwetting phase reservoir by increasing or decreasing the through-flow rate. The pressure in the wetting phase reservoir was always atmospheric. By increasing the pressure of the nonwetting phase reservoir, drainage could be initiated. At the end of, or during, a drainage event, imbibition could be brought about by reducing the pressure of the nonwetting phase reservoir.

5. Quasi-Static Experiments

[55] The micromodels used in this set of experiments had 3000 pore bodies, nearly 9000 pore throats, and the mean pore size was 40 μm. Their depth was equal to 40 μm. The micromodel was initially saturated with the wetting phase, which was Fluorinert FC-43. The nonwetting phase was water dyed with ink. The pressure of the nonwetting phase was increased, until it was just high enough for the nonwetting phase to enter the flow network. The spatial configuration of the fluids in the micromodel was continuously monitored and when there was no change (usually after 20 min), we assumed that equilibrium was reached. By stepwise increase of the nonwetting phase pressure with 50 Pa, subsequent stages of drainage were achieved. At every equilibrium step, a snapshot of the fluids configuration in the network was acquired. The drainage experiment was over once the nonwetting phase reached the end of the micromodel and entered the outflow reservoir (i.e., breakthrough). Then, quasi-static imbibition experiment was carried out by stepwise decrease of the nonwetting phase pressure. All experiments were conducted in a constant-temperature room at 21 ± 1°C.

6. Results

[56] The acquired images were analyzed with IDL software package (IT&T Visual Information Solutions) to calculate saturation and the specific interfacial area between Fluorinert and dyed water at an imposed capillary pressure. Results were used to plot capillary pressure-saturation curves as well as capillary pressure-saturation-interfacial area surfaces.

[57] In Figure 11, data points for capillary pressure and saturation for a series of drainage-imbibition cycles are shown. It is obvious that the capillary pressure-saturation relationship is highly hysteretic. These results clearly show that the knowledge of pressure and saturation is not enough to fully specify the state of the system.

[58] The hysteretic behavior of the system can also be seen in Figure 12, where two images from the same part of the network. Left image is from imbibition and the right one is from drainage. The phase saturation is nearly the same in both images, but the capillary pressure is

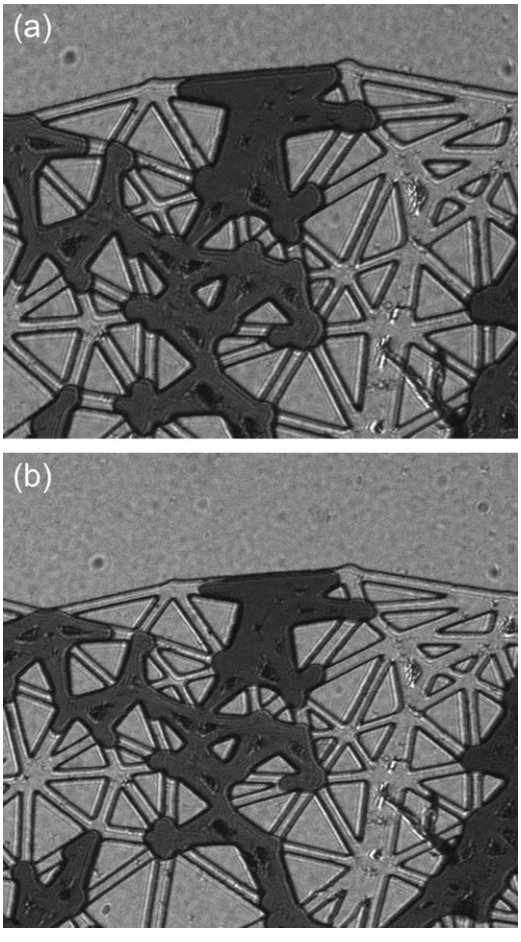

Figure 12. Images from a small part of the network at (left) drainage and (right) imbibition. In both images, the wetting phase saturation is 72%. In the left picture, the capillary pressure is 4833 Pa, while in the right picture the applied pressure is 2160 Pa.

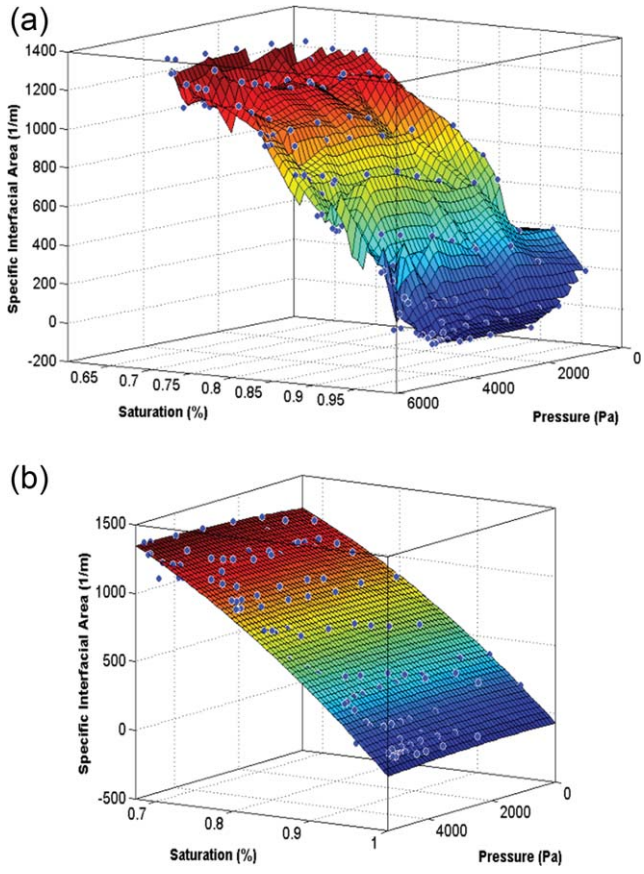

Figure 13. From left to right, the surfaces that were formed by data points obtained during drainage and imbibition, both interpolated and fitted, are presented.

significantly different. In the left picture, the capillary pressure is 4833 Pa, while in the right picture the applied pressure is 2160 Pa. But, also the interfacial areas of the two images are significantly different (2.8×10^{-7} m^2 and 7.4×10^{-7} m^2, respectively).

[59] In quasi-two-dimensional micromodels, like the one that we used in our experiments, there is very limited corner flow of the wetting phase. The only parts of the network where the wetting phase stays connected with the wetting phase reservoirs are the corners along the upper and lower side boundaries of the network. The wetting phase in all other corners remains isolated due to the two-dimensional nature of the micromodel. The flow through these side boundary corners was negligible because of their limited volume, and the system exhibited a highly hysteretic behavior. As soon as the pressure was low enough for the nonwetting phase to free the upper and lower boundaries of the network, then imbibition was very fast.

[60] As it was mentioned above, theoretical, numerical, and experimental results have shown that it is crucially important to include interfacial area for a complete description of two-phase flow in porous media [see e.g., *Hassanizadeh and Gray*, 1990, 1993b; *Held and Celia*, 2001; *Cheng et al.*, 2004; *Joekar-Niasar et al.*, 2010b; *Joekar-Niasar and Hassanizadeh*, 2011, 2012].

[61] In Figure 13a, all equilibrium data of saturation, capillary pressure, and specific interfacial area from imbibition and drainage experiments are plotted. In Figure 13b, a surface fitted to these date points is shown. The fitted surface can be described by the following function [after *Joekar-Niasar and Hassanizadeh*, 2012]:

$$a^{wn} = \alpha \cdot S \cdot (1 - S)^{\beta} \cdot P_c^{\gamma}$$

[62] The choice of such a fitting function was made so that at a wetting phase saturation of zero, there will be zero interfacial area. In Table 1, the values for the fitting parameters, their confidence levels, as well as R^2 values are given. These parameter values are obtained if specific interfacial area and capillary pressure are given in S.I. units.

[63] As it can be seen in the table, there was a very good match for the fitting of all data points by a single surface.

[64] We also fitted individual surfaces to drainage and imbibition data points separately. The maximum difference between the two surfaces was found to be about 8%, while on average, the mean difference was around 4%. The reason for the difference between the two individual surfaces, one for drainage and one for imbibition was the creation of disconnected nonwetting phase after primary drainage. The disconnection of the nonwetting phase created interfaces that in future steps, a part of it would get reconnected, and a part of it would remain disconnected.

[65] It can be seen in Figure 14, where snapshots of the same part of the micromodel during primary drainage (left image) and main imbibition (right image) are shown, that the disconnection of the nonwetting phase created many interfaces. A big part of the disconnected phase would get reconnected, but not all of it. The wetting phase saturation was almost the same in the two situations (83.4% and 84.0%, respectively). But, the values of capillary pressure and interfacial area were significantly different. For the left image, the pressure was 4833 Pa and the interfacial area was roughly 2.8×10^{-7} m^2. For the right side, the pressure was 1080 Pa (thus lower) whereas the interfacial area was around 2.1×10^{-6} m^2 (i.e., much higher).

7. Discussion

[66] The experimental results showed that the relation between capillary pressure and saturation for drainage and imbibition is hysteretic; we have many possible equilibrium curves. However, the inclusion of interfacial area as a new state variable can eliminate hysteresis. Instead of many curves, we get one unique surface, which is the locus of all drainage and imbibition data points. This also means that we can estimate a unique value of interfacial area for every capillary pressure-saturation pair. This surface is unique for a given set of fluids and solid phases and a given percolation pattern. In fact, after repeating the experiment many times, for the same pressure steps, the same

Table 1. The Fitting Parameters for the Pc-Sw-Awn Surface

Parameter	Value	Confidence levels
α	2538.59	2315.79–2759.65
β	1.185	1.165–1.205
γ	0.004594	−0.0059 to 0.0151
R^2	0.992	

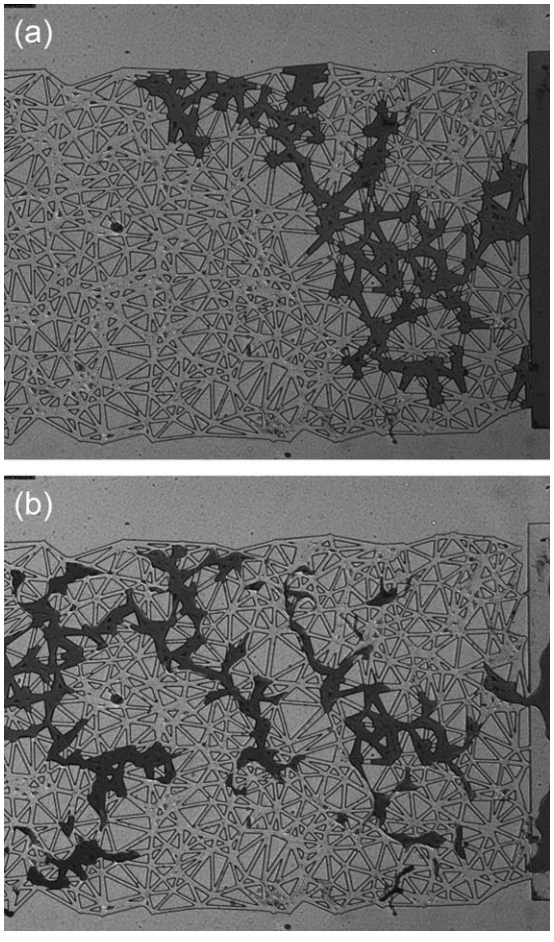

Figure 14. The configuration of fluids in (left) drainage and (right) imbibition in the same part of the flow network.

percolation patterns were obtained. When the pressure steps were slightly increased, then the distribution of fluids in the network were different. But, we still obtained the same P_c-S-a^{wn} surface. When the experiment was repeated with different pairs of liquids (we used perfluorodecalin and water), the pattern was different from the one with fluorinert and water, but still reproducible under the same conditions. Of course, we got a different P_c-S-a^{wn} surface than for water and fluorinert.

[67] Finally, we verified our initial claim that our flow domain comprised four REVs. We divided the flow domain into four subdomains and compared the capillary pressure-saturation–specific interfacial area surfaces of subdomains with each other as well as with the surface for the whole domain. The results showed that the fitted surfaces matched well, with the highest mismatch being less than 4%.

8. Conclusions

[68] We have developed a relatively simple and highly effective method for constructing PDMS micromodels. Through a series of steps, which in total take less than a week, we can construct a fully functional micromodel. The most time-consuming part is the production of the master wafer, which takes almost six days, including the preparation of the mask and shipping. After that, the micromodel can be ready in 4–5 h. Up to now, PDMS micromodels were not considered to be suitable for well-controlled two-phase flow experiments because of their mixed wettability, and the fact that it changes with time. We have developed a reliable procedure for making PDMS micromodels that are uniformly and stably hydrophobic. This is a major improvement in addressing wettability problems of PDMS and makes it a very attractive alternative to other materials, like photoresist, silicon, glass, or quartz. In comparison to previous experimental work on the significance of the inclusion of interfacial area as a separate variable, we may make the following observations. It is the first time that an elongated micromodel is being used. This offered the ability to study the concept of REV, and to verify its average properties related to interfacial area experimentally. It was observed and verified that corner flow is not present in a two-dimensional micromodel, except from the upper and lower boundaries of the flow network. This caused the capillary pressure–saturation curve to be highly hysteretic. The network configuration allowed for the existence of residual saturation for, wetting and nonwetting phases. Because we did not have corner flow, the lowest wetting phase saturation we could reach was around 60%. Therefore, we could not reach maximum values of the specific interfacial area. So, in comparison to other two-dimensional micromodels, the interfacial area that we measured was relatively smaller.

[69] We have shown that the visualization setup, using four cameras, can provide dynamic images of the distribution of two immiscible liquids over the whole length of the micromodel. By performing quasi-static experiments, we have shown the validity of the hypothesis that capillary pressure-saturation-interfacial area data points form a unique surface for all drainage and imbibition processes.

[70] **Acknowledgments.** The authors would like to acknowledge three anonymous reviewers and the Associate Editor, Markus Hilpert, for valuable comments and suggestions. N. K. Karadimitriou and S. M. Hassanizadeh are members of the International Research Training Group NUPUS, financed by the German Research Foundation (DFG) and The Netherlands Organization for Scientific Research (NWO). This research project was financed by NWO Grant No. 818.01.008.

References

Avraam, D. G., G. B. Kolonis, T. C. Roumeliotis, G. N. Constantinides, and A. C. Payatakes (1994), Steady-state two-phase flow through planar and nonplanar model porous media, *Transp. Porous Media*, *16*(1), 0169–3913, 75–101, doi:10.1007/BF01059777.

Baouab, Z., M. Najjari, H. Ouerfelli, S. Ben Nasrallah (2007), Experimental study of the effects of hydraulic gradient and injected-gas flow rate on fragmentation in porous media, *J. Pet. Sci. Eng.*, *59*, 250–256.

Baumann, T., and C. J. Werth (2004), Visualisation and modelling of polystyrol colloid transport in a silicon micromodel, *Vadose Zone J.*, *3*, 434–443.

Bietsch, A., and B. Michel (2000), Conformal contact and pattern stability of stamps used for soft lithography, *J. Appl. Phys.*, *88*, 4310.

Bodas, D., and C. Khan-Malek (2007), Hydrophilization and hydrophobic recovery of PDMS by oxygen plasma and chemical treatment—An SEM investigation, *Sensors Actuators B Chem.*, *123*, 368–373.

Chang, L.-C., J.-P. Tsai, H.-Y. Shan, and H.-H. Chen (2009), Experimental study on imbibition displacement mechanisms of two-phase fluid using micro model, *Environ. Earth Sci.*, *59*, 901–911, doi:10.1007/s12665-009-0085-6.

Chen, D., L. J. Pyrak-Nolte, J. Griffin, and N. J. Giordano (2007), Measurement of interfacial area per volume for drainage and imbibition, *Water Resour. Res.*, *43*, W12504, doi:10.1029/2007WR006021.

Cheng, J.-T. (2002), Fluid flow in ultra-small capillaries, Ph.D. Thesis, Purdue Univ., Lafayette, Indiana.

Cheng, J.-T., L. J. Pyrak-Nolte, D. D. Nolte, and N. J. Giordano (2004), Linking pressure and saturation through interfacial areas in porous media, *Geophys. Res. Lett.*, *31*, L08502, doi:10.1029/2003GL019282.

Corapcioglu, M. Y., S. Yoon, and S. Chowdhury (2009), Pore-scale analysis of NAPL blob dissolution and mobilization in porous media, *Transp. Porous Media*, *79*(3), 419–442, doi:10.1007/s11242-008-9331-8.

Dangla, R., F. Gallaireb, and C. N. Baroud (2010), Microchannel deformations due to solvent-induced PDMS swelling, *Lab Chip*, *10*(21), 2972–2978.

Duffy, D. C., J. C. M. Olivier, J. A. Schueller, and G. M. Whitesides (1998), Rapid prototyping of microfluidic systems in poly(dimethylsiloxane), *Anal. Chem.*, *70*, 4974–4984.

Duffy, D. C., O. J. A. Schueller, S. T. Brittain, and G. M. Whitesides (1999), Rapid prototyping of microfluidic switches in poly(dimethyl siloxane) and their actuation by electro-osmotic flow, *J. Micromech. Microeng.*, *9*, 211–217.

Eddings, M. A., and B. K. Gale (2006), A PDMS-based gas permeation pump for on-chip fluid handling in microfluidic devices, *J. Micromech. Microeng.*, *16*, 2396–2402.

Eddings, M. A., M. A. Johnson, and B. K. Gale (2008), Determining the optimal PDMS-PDMS bonding technique for microfluidic devices, *J. Micromech. Microeng.*, *18*(6).

Er, V., T. Babadagli, and Z. Xu (2010), Pore-scale investigation of the matrix−fracture interaction during co2 injection in naturally fractured oil reservoirs, *Energy Fuels*, *24*(2), 1421–1430.

Ferer, M., C. Ji, G. S. Bromhal, J. Cook, G. Ahmadi, and D. H. Smith (2004), Crossover from capillary fingering to viscous fingering for immiscible unstable flow: Experiment and modelling, *Phys. Rev. E*, *70*(1).

Fritz, J. L., and M. J. Owen (1995), Hydrophobic recovery of plasma-treated polydimethylsiloxane, *J. Adhesion*, *54*, 33–45.

Gervais, T., J. El-Ali, A. Gunther, and K. F. Jensen (2006), Flow-induced deformation of shallow microfluidic channels, *Lab Chip*, *6*, 500–507.

Go, J. S., and S. Shoji (2004), A disposable, dead volume-free and leak-free in-plane PDMS microvalve, *Sensors Actuators A*, *114*, 434–44.

Grate, J. W., C. Zhang, T. W. Wietsma, M. G. Warner, Anheier Jr., N. C., B. E. Bernacki, G. Orr, and M. Oostrom (2010), A note on the visualization of wetting film structures and a nonwetting immiscible fluid in a pore network micromodel using a solvatochromic dye, *Water Resour. Res.*, *46*, W11602, doi:10.1029/2010WR009419.

Gutiérrez, B., F. Juarez, L. Ornelas, S. Zeppieri, A. López de Ramos (2008), Experimental study of gas–liquid two-phase flow in glass micromodels, *Int. J. Thermophys.*, *29*, 2126–2135, doi:10.1007/s10765-007-0305-9.

Hassanizadeh, S. M., and W. G. Gray (1990), Mechanics and thermodynamics of multiphase flow in porous media including interphase boundaries, *Adv. Water Resour.*, *13*, 169–186.

Hassanizadeh, S. M., and W. G. Gray (1993a), Toward an improved description of the physics of 2-phase flow, *Adv. Water Resour.*, *16*(1), 53–67.

Hassanizadeh, S. M., and W. G. Gray (1993b), Thermodynamic basis of capillary pressure in porous media, *Water Resour. Res.*, *29*(10), 3389–3405.

Haubert, K., T. Drier, and D. Beebe (2006), PDMS bonding my means of a portable, low-cost corona system, *Lab Chip*, *6*, 1548–1549.

Heiba, A. A., M. Sahimi, L. E. Scriven, and H. T. Davis (1992), Percolation theory of two-phase relative permeability, paper SPE 11015 presented at the 57th Annual Fall Meeting of the Society of Petroleum Engineers, Society of Petroleum Engineers, New Orleans, La.

Held, R. J., and M. A. Celia (2001), Modeling support of functional relationships between capillary pressure, saturation, interfacial area and common lines, *Adv. Water Resour.*, *24*, 325–343.

Hug, T. S., D. Parrat, P.-A. Kunzi, U. Staufer, E. Verpoorte, and N. F. de Rooij (2003), Fabrication of nanochannels with PDMS, silicon and glass walls and spontaneous filling by capillary forces, paper presented at 7th International Conference on Miniaturized Chemical and Blochemlcal Analysts Systems, Tahoe City, Calif.

Huh, D., K. L. Mills, X. Zhu, M. A. Burns, M. A. Thouless, and S. Takayama (2007), Tuneable elastomeric nanochannels for nanofluidic manipulation, *Nature Mater.*, *6*, 424–428, doi:10.1038/nmat1907.

Joekar-Niasar, V., and S. M. Hassanizadeh (2011), Specific interfacial area; the missing state variable in two-phase flow equations, *Water Resour. Res.*, *47*, W05513, doi:10.1029/2010WR009291.

Joekar-Niasar, V., and S. M. Hassanizadeh (2012), Uniqueness of specific interfacial area–capillary pressure–saturation relationship under non-equilibrium conditions in two-phase porous media flow, *Transp. Porous Media*, doi:10.1007/s11242-012-9958-3.

Joekar-Niasar, V., S. M. Hassanizadeh, L. J. Pyrak-Nolte, and C. Berentsen (2010a), Simulating drainage and imbibition experiments in a high-porosity micro-model using an unstructured pore-network model, *Water Resour. Res.*, *45*, W02430, doi:10.1029/2007WR006641.

Joekar-Niasar, V., M. Prodanovic, D. Wildenschild, and S. M. Hassanizadeh (2010b), Network model investigation of interfacial area, capillary pressure and saturation relationships in granular porous media, *Water Resour. Res.*, *46*, W06526, doi:10.1029/2009WR008585.

Johnston, W. G. (1962), Dislocation etch pits in non-metallic crystals with bibliography, in *Progress in Ceramic Science, vol. 2*, edited by J. E. Burke, pp. 1–75. Pergamon, N. Y.

Karadimitriou, N. K., and S. M. Hassanizadeh (2012), A review of micromodels and their use in two-phase flow studies, *Vadose Zone J.*, *11*(3).

Karadimitriou, N. K., V. Joekar-Niasar, S. M. Hassanizadeh, P. J. Kleingeld, and L. J. Pyrak-Nolte (2012), A novel deep reactive ion etched (DRIE) glass micro-model for two-phase flow experiments, *Lab Chip*, *12*, 3413–3418.

Lee, J., C. Park, and G. M. Whitesides, (2003), Solvent compatibility of poly(dimethylsiloxane)-based microfluidic devices, *Anal. Chem.*, *75*, 6544–6554.

Liu, Y., D. D. Nolte, and L. J. Pyrak-Nolte (2011), Hysteresis and interfacial energies in smooth-walled microfluidic channels, *Water Resour. Res.*, *47*, W01504, doi:10.1029/2010WR009541.

McKellar, M., and N. C. Wardlaw (1982), A method of making two-dimensional glass micromodels of pore system, *J. Can. Pet. Technol.*, *21*(4), 1–3.

Murakami, S.-I., T. Kuroda, and Z. Osawa, (1998), Dynamics of polymeric solid surfaces treated with oxygen plasma: Effect of aging media after plasma treatment, *J. Colloid Interface Sci.*, *202*, 37–44.

NagaSiva, G., B. Bera, N. K. Karadimitriou, S. K. Mitra, and S. M. Hassanizadeh (2011), Reservoir-on-a-chip (ROC): A new paradigm in reservoir engineering, *Lab Chip*, *11*, 3785–3792, (Featured Article), doi:10.1039/C1LC20556K.

Ohara, J., K. Asami, Y. Takeuchi, and K. Sato (2010), Development of RIE-lag reduction technique for si deep etching using double protection layer method, *IEE J. Trans. Electr. Electron. Eng.*, *5*, 125–130, doi:10.1002/tee.20506.

Pyrak-Nolte, L. J., D. D. Nolte, D. Chen, and N. J. Giordano (2008), Relating capillary pressure to interfacial areas, *Water Resour. Res.*, *44*, W06408, doi:10.1029/2007WR006434.

Samel, B., M. K. Chowdhury, and G. Stemme, (2007), The fabrication of microfluidic structures by means of full-wafer adhesive bonding using a poly(dimethylsiloxane) catalyst, *J. Micromech. Microeng.*, *17*, 1710–1714.

Satyanarayana, S., R. N. Karnik, and A. Majumdar, (2005), Stamp-and-stick room-temperature bonding technique for microdevices, *J. Microelectromech Syst.*, *14*, 392–399.

Wegner, M. W., and J. M. Christie (1983), Chemical etching of deformation substructures in quartz, *Phys Chem. Miner.*, *9*, 67–78.

Willingham, T. W., C. J. Werth, and A. J. Valocchi (2008), Evaluation of the effects of porous media structure on mixing-controlled reactions using pore-scale modeling and micromodel experiments, *Environ. Sci. Technol.*, *42*(9), 3185–3193.

Xia, Y., and G. M. Whitesides (1998), Soft Lithography. *Angewandte Chemie Int. Ed.*, *37*, 550–575.

Yeom, J., Y. Wu, J. C. Selby, and M. A. Shannona (2005), Maximum achievable aspect ratio in deep reactive ion etching of silicon due to aspect ratio dependent transport and the microloading effect, *J. Vac. Sci. Techno. B Microelectron. Nanometer Struct.*, *23*(6), 2319–2329, doi:10.1116/1.2101678.

Zhang, C., M. Oostrom, T. W. Wietsma, J. G. Grate, and M. G. Warner (2011), Influence of viscous and capillary forces on immiscible fluid displacement: Pore-scale experimental study in a water-wet micromodel demonstrating viscous and capillary fingering, *Energy Fuels*, *25*(8), 3493–3505, doi:10.1021/ef101732k.